Towards spin-polarized two-dimensional electron gas at a surface of an antiferromagnetic insulating oxide

Rohan Mishra, Young-Min Kim, Qian He, Xing Huang, Seong Keun Kim, Michael A. Susner, Anand Bhattacharya, Dillon D. Fong, Sokrates T. Pantelides, and Albina Y. Borisevich

Phys. Rev. B **94**, 045123 — Published 18 July 2016

DOI: 10.1103/PhysRevB.94.045123

Towards Spin-polarized Two-dimensional Electron Gas at a Surface of an Antiferromagnetic Insulating Oxide

Rohan Mishra,[1,2,3,*] Young-Min Kim,[2,4] Qian He,[2] Xing Huang,[3] Seong Keun Kim,[5,6] Michael A. Susner,[2] Anand Bhattacharya,[5,7] Dillon D. Fong,[5] Sokrates T. Pantelides,[1,2] Albina Y. Borisevich[2]

[1]*Deparment of Physics and Astronomy, Vanderbilt University, Nashville, Tennessee 37235, USA*

[2]*Materials Science and Technology Division, Oak Ridge National Laboratory, Oak Ridge, Tennessee 37831, USA*

[3]*Department of Mechanical Engineering and Materials Science, and Institute of Materials Science and Engineering, Washington University in St. Louis, St. Louis, Missouri 63130, USA*

[4]IBS Center for Integrated Nanostructure Physics (CINAP), Institute for Basic Science, *Department of Energy Science, Sungkyunkwan University, Suwon 440-746, Republic of Korea*

[5]*Materials Science Division, and* [7]*Nano Science and Technology Division, Argonne National Laboratory, Argonne, Illinois 60439, USA*

[6]*Center for Electronic Materials, Korea Institute of Science and Technology, Seoul, 02792, Republic of Korea*

To whom all correspondence should be addressed *rmishra@wustl.edu

RM and YMK contributed equally to this work.

Abstract: The surfaces of transition-metal oxides with the perovskite structure are fertile grounds for the discovery of novel electronic and magnetic phenomena. In this article, we combine scanning transmission electron microscopy (STEM) with density functional theory (DFT) calculations to obtain the electronic and magnetic properties of the (001) surface of a $(LaFeO_3)_8/(SrFeO_3)_1$ superlattice film capped with four layers of $LaFeO_3$. Simultaneously acquired STEM images and electron-energy-loss spectra reveal the surface structure and a reduction in the oxidation state of iron from Fe^{3+} in the bulk to Fe^{2+} at the surface, extending over several atomic layers, which signals the presence of oxygen vacancies. DFT calculations confirm the reduction in terms of oxygen vacancies and further demonstrate the stabilization of an exotic phase in which the surface layer is half-metallic and ferromagnetic, while the bulk remains antiferromagnetic and insulating. Based on the calculations, we predict that the surface magnetism and conductivity can be controlled by tuning the partial pressure of oxygen.

1. Introduction

The breaking of symmetry in transition-metal oxides (TMOs), such as at an interface with another material or at a surface leads to novel physical phenomena [1]. While oxide interfaces have been studied widely, their surfaces are starting to garner interest only recently with reports of observation of two-dimensional electron gas (2DEG) [2-4], superconductivity [5], and chiral magnetism [6]. Oxide surfaces also display excellent activity for water-splitting and are promising candidates to replace the expensive noble metal catalysts that are currently in use [7,8]. Moreover, due to the strong coupling between the functionalities of oxides and external parameters such as electric or magnetic fields and oxygen partial pressure [9-11], it may also be possible to tune the properties of oxide surfaces for novel applications [12-14].

Control over the functionalities of oxide surfaces, however, requires extensive quantitative information about their structure and behavior at the atomic scale to enable the construction of a comprehensive, predictive theoretical model. The chemical complexity of TMOs together with the presence of competing order parameters makes atomic-scale characterization of their surfaces a particularly challenging task and is one of the reasons that oxide surfaces have not received as much attention as oxide interfaces. Scanning tunneling microscopy (STM) [15] is an excellent technique to map the atomic and electronic structure of metals. STM has been used to characterize the surface of heavily doped $SrTiO_3$ [16] and, more recently, of metallic perovskites such as $SrRuO_3$ [17] and mixed-valence manganites ($A_{1-x}Ca_xMnO_3$, where A = Bi, La) [18-20]. Many widely-studied TMOs are, however, wide-bandgap insulators and as a result are unsuitable for STM characterization. As is the case with *sp*-bonded semiconductors and binary oxides, TMO surfaces undergo reconstruction, with implications on the structure, chemistry, and properties of one or more sub-surface layers. While STM can give very good information about the details of surface reconstruction, altered properties of subsurface layers cannot be examined, even for conductive surfaces. Transmission electron microscopy (TEM) performed in cross-section provides an alternative route to overcome these challenges and has been used to characterize surfaces of metals, alloys, binary oxides [21-25], and a few insulating TMOs, namely $SrTiO_3$ [21,22,26] and $LaAlO_3$ [23,27].

In this article, we combine aberration-corrected scanning transmission electron microscope (STEM) imaging and electron energy loss spectroscopy (EELS) [28] with first-principles density functional theory (DFT) calculations to characterize the electronic and magnetic properties of the (001) surface of a $(LaFeO_3)_8/(SrFeO_3)$ superlattice capped with four layers of $LaFeO_3$. From STEM imaging, we find the surface of the film to be terminated with a LaO layer. From STEM EELS, we observe a reduction in the oxidation state of iron from 3+ in the bulk to 2+ at the surface, which is indicative of the formation of oxygen vacancies. The reduced region extends over approximately four unit cells from the

surface (~1.5 nm). We combine the structural information gathered from STEM/EELS with DFT calculations to obtain further information about the electronic and magnetic properties of reduced $LaFeO_3$ surfaces. We find that the electrons introduced by the LaO-termination and by oxygen vacancies in the reduced surface region are localized at the surface $LaFeO_3$ unit cell. Based on the DFT calculations, we predict that the system is close to a phase transition: by introducing additional oxygen vacancies at the surface and consequently reducing the surface below Fe^{2+}, it is possible to stabilize an exotic phase where the surface layer displays a half-metallic ferromagnetic behavior with a spin-polarized two-dimensional electron gas (2DEG), while the bulk remains antiferromagnetic and insulating. Overall, our results demonstrate that the combination of STEM/EELS with DFT calculations provides a powerful tool to characterize the electronic properties of TMO surfaces and enable their engineering for novel applications.

2. Methods

***Film Growth*:** The $(LaFeO_3)_8/(SrFeO_3)_1$ superlattice film was grown on the TiO_2-terminated $SrTiO_3$ (001) single crystal by ozone-assisted molecular beam epitaxy. The superlattice was grown at a substrate temperature of 650 ^oC under ozone pressure of 2 x 10^{-6} Torr. The layering sequence was deposited as $[(LaO/FeO_2)\times4 + (SrO/FeO_2) + (LaO/FeO_2)\times4]$ and repeated 4 times. The superlattice periodic structure was monitored by in-situ reflection high-energy electron diffraction.

***STEM and EELS Characterization*:** Cross-sectional samples were used for the study and were prepared using conventional mechanical polishing and ion-milling process. STEM ADF and ABF imaging were carried out in an aberration-corrected Nion UltraSTEM200 microscope operating at 200 kV, while STEM-EELS measurements were carried out in a Nion UltraSTEM100 microscope operated at 100 kV equipped with a Gatan Enfina EEL spectrometer. Both the microscopes are equipped with a 5th order aberration corrector. The EELS collection semi-angle was 48 mrad and the EEL spectra were recorded from 490 to 892 eV with 0.3 eV/ch and 0.5 sec/pixel dwell time. The STEM specimen thickness was kept within 0.3-0.4 inelastic mean free paths (25-35 nm). We followed the procedure used in Refs. [29,30] to extract the Fe L_3/L_2 ratio. We first performed principal component analysis (PCA) on the EEL spectrum to remove random noise. We then removed the background below the Fe $L_{3,2}$ peak using a power-law fit from (663 – 703) eV. We used a Hartree-Slater cross-section function available in Digital Micrograph [31] to approximate the continuum contribution. The L_3/L_2 ratio was determined using the following equation:

$$\frac{L_3}{L_2} = \frac{\int L_3 - \frac{\int \text{Region1}}{\int \sigma(\text{Region1})} \times \int \sigma(L_3)}{\int L_2 - \frac{\int \text{Region1}}{\int \sigma(\text{Region1})} \times \int \sigma(L_2)}, \qquad \text{Eq. (1)}$$

where, $\int L_3$, $\int L_2$, and $\int \mathrm{Region1}$ are the integrated areas under L_3 peak (707-714.5 eV), L_2 peak (719.5-727 eV), and a scaling window referred to as Region1 (727.3-734.8 eV), respectively, and $\int \sigma(L_3)$, $\int \sigma(L_2)$, and $\int \sigma(\mathrm{Region1})$ are the integrated area under the Hartree-Slater cross-section under L_3, L_2 and Region1, respectively. This procedure was also used to extract the L_3/L_2 ratio of the reference specimens.

***DFT Calculations*:** DFT calculations were performed using a plane-wave basis set with a cut-off energy of 500 eV and the projector-augmented-wave method (PAW) [32] as implemented within the Vienna *ab initio* simulation package (VASP) code [33,34]. Electron exchange and correlation effects were described within the spin-polarized Perdew-Burke-Ernzerhof (PBE) functional [35]. We used slabs with a (2×2×5) supercell of the 5-atom perovskite unit-cell and ~15 Å of vacuum for the calculations. The slabs were symmetrical with both the surface having either FeO_2 or LaO termination. To simulate the epitaxial growth on $SrTiO_3$, the in-plane lattice constants were constrained to match the theoretical $SrTiO_3$ lattice constant of 3.952 Å. In order to simulate a thick slab, the atoms in the middle layer of the slab were fixed to the atomic positions within bulk $LaFeO_3$ (with $a^-a^-c^+$ tilt) strained to $SrTiO_3$. The ions in the remaining layers were allowed to relax until forces per ion were smaller than 10 meV/Å. The Brillouin zone was sampled using a 2×2×1 Monkhorst−Pack *k*−points mesh [36] for relaxations and a denser 6×6×1 *Γ*-centered mesh for electronic calculations. Further, transition-metal atoms, such as Fe, have localized *d*-electrons giving rise to strong correlations which are usually not correctly described by GGA [37]. To address this issue we have included the effect of strong correlations by using the DFT+*U* approach[37]. Specifically, we used the rotationally invariant Dudarev approach [38] to DFT+*U*, in which only one effective Hubbard parameter $U_{\mathrm{eff}} = U - J$ is used, with *U* and *J* being Hubbard repulsion and intra-atomic exchange, respectively for the electrons in the localized *d*-states. We used U_{eff} of 5.1 eV for Fe for the electronic calculations, based on the work by Hong *et al*. [39]. The formation energies of oxygen vacancies have also been calculated using GGA+*U*, as the vacancy formation energy obtained using GGA have been shown to be significantly higher than the experimental values in bulk $La_xSr_{1-x}FeO3_{-\delta}$ [40] solid solutions. We also repeated some of the calculations with a (2×2×7) slab with seven-perovskite unitcells thickness and find the results to be in agreement with those obtained for the (2×2×5) slab.

We followed the procedure used in Ref. [41,42] to calculate the oxygen vacancy formation energy with respect to the stoichiometric LaO or FeO_2 surface without vacancies. The formation energy of *n* oxygen vacancies in $LaFeO_3$ can be expressed by:

$$\Delta E_f = \frac{1}{n}\left(E_{\mathrm{LaFeO_{3-n}}} - E_{\mathrm{LaFeO_3}} + \frac{n}{2} G_{\mathrm{O_2}} \right), \qquad \text{Eq. (2)}$$

where, $E_{\mathrm{LaFeO_{3-}}_n}$ and $E_{\mathrm{LaFeO_3}}$ are the calculated energies of a $LaFeO_3$ slab with *n* oxygen vacancies and without any vacancies, respectively, and $G_{\mathrm{O_2}}$ is the Gibbs free energy of an oxygen molecule. We have neglected the vibrational and configurational entropy contributions to the free energy of the $LaFeO_3$ slab as the difference in their values with and without vacancies is found to be minimal [43,44].

The free energy of the oxygen molecule is defined as [42,45]:

$$G_{\mathrm{O_2}} = \mu_{\mathrm{O_2}}\left(T,P\right) = \mu_{\mathrm{O_2}}\left(T,P^0\right) + E_{\mathrm{O_2}} + kT\ln\left(P/P^0\right), \qquad \text{Eq. (3)}$$

where, $\mu_{\mathrm{O_2}}\left(T,P\right)$ is the experimentally measured chemical potential of oxygen molecule at any given temperature *T* and partial pressure *P*, $E_{\mathrm{O_2}}$ is the DFT calculated energy of an oxygen molecule in vacuum in triplet state, *k* is the Boltzmann's constant, and P^0 is 1 atm.

3. Results and Discussion

A high-angle annular dark-field (HAADF) STEM image of the ~15 nm thick $(LaFeO_3)_8/(SrFeO_3)$ superlattice film oriented along the $[110]_{pc}$ direction (pc denotes pseudocubic) is shown in Fig. 1(a). As the contrast in a HAADF STEM image is roughly proportional to Z^2 [28], with *Z* being the atomic number, the cation columns in the thin film can be clearly observed in Fig. 1(a), while the oxygen columns are invisible ($Z = 8$) due to dynamic range constraints. Since Sr is lighter than La, the SrO layers appear darker.

Figure 1(b) shows a HAADF image of a magnified region of the film surface, which appears terminated by a LaO layer. A clearer picture of the surface appears in a simultaneously acquired phase-contrast image formed on an annular bright-field (ABF) detector [46] as shown in Fig. 1(c). In addition to the LaO-terminated surface layer, the sub-surface FeO_2 layer is also visible in the ABF image. Moreover, the oxygen columns in the FeO_2 layer lying in between Fe atoms also appear as a set of extra spots (compared to the HAADF image). The oxygen columns do not lie in the same straight line with Fe columns due to the presence of octahedral tilts along $[100]_{pc}$ and $[010]_{pc}$ directions [47], in agreement with the reported *Pbnm* symmetry of $LaFeO_3$ in bulk [48] and thin-film form [49]; remarkably, this effect appears to persist up to the surface unit cell. Overall, STEM imaging provides essential information about the surface termination and the octahedral tilt pattern of the film.

In order to map the chemistry of the surfaces, we performed EELS line scans on the film. Figure 2(a) shows an ADF image of a representative region where EELS scans were performed focused in an energy loss window of (490-890) eV to study the variations in O *K*, Fe *L* and La *M* edges within the film. On moving from the bulk of the film towards its surface, we observed significant changes in the Fe *L* edge.

The Fe *L* edge arises from transitions of *2p* core electrons to final states with *s* and 3*d* orbital content, whereby the shape and position of the peaks are sensitive to the oxidation state and the local bonding environment of the Fe atoms [50]. The edge is composed of the L_3 peak with an onset at ~708 eV and the L_2 peak with an onset at ~720 eV. The separation between the two peaks is a consequence of the spin-orbit splitting of the core *2p* states from where the electrons are excited. The L_3 peak undergoes further splitting into two peaks depending on the coordination of the oxygen atoms around iron (referred to as crystal-field splitting). It is known [30,50] that on reduction from Fe^{3+} to Fe^{2+}, the maximum of the L_3 peak shifts lower in energy from 710 eV to 708 eV, respectively.

The reduction of Fe^{3+} to Fe^{2+} is also associated with an increase in the intensity of the L_2 peak with respect to the L_3 peak, and the change in the ratio of the L_3 to L_2 peak intensity (Fe L_3/L_2 ratio) shows a linear trend with reduction [30]. Figure 2(b) shows the Fe *L* peaks obtained from the top five layers from the surface of the film. On comparing them with reference spectra obtained from bulk compounds with Fe^{2+} and Fe^{3+} (see Supplemental Material [51] for details on the standard specimens), we find that the surface of the film is reduced from ~$Fe^{(3+,4+)}$ in the bulk of the film to ~Fe^{2+} in the surface region. This region extends to roughly four unit cells from the surface. In order to quantify the change in oxidation state, we used the EELS data to extract the Fe L_3/L_2 ratio [29,30] across the thickness of the film; it is displayed in Fig. 2(c). The L_3/L_2 ratio shows a dip in the regions that have a layer of $SrFeO_3$. Addition of Sr increases the Fe oxidation state above 3+ and previous EELS studies on Fe^{4+}compounds show that L_3/L_2 ratio decreases on moving from Fe^{3+} to Fe^{4+} [52]. However, in contrast to Fe^{2+} compounds where the L_3 peak shifts to lower energy, in Fe^{4+} compounds it remains at the same energy as in Fe^{3+} (see Supplemental Material Fig. S2). Thus, the Fe *L* edge EELS results provide strong evidence of reduction of the surface of the film from a combination of 3+ and 4+ oxidation states to 2+ at the surface, with the reduction being confined to four unit cells of the surface.

Besides the distinctive changes in the Fe $L_{3,2}$ edge, O *K* edge also conveys information on the oxidation state of Fe. Fig. 3 shows O *K* edge fine structure for the upper part of the film including the surface. The first peak (denoted by A) around 530 eV has been attributed to transitions from 1*s* core states to unoccupied O 2*p* states hybridized with Fe 3*d* states [53,54]. The second peak (denoted by B) around 535 eV has been attributed to transitions to empty O 2*p* states hybridized with La *d* states [55]. Suppression of peak A, and change in separation between the A and B peaks (ΔE = B-A) have been recognized as indicators of change in oxidation state of the transition-metal cations in perovskites [29,56,57]. For the superlattice film, a suppression of peak A and the decrease in ΔE at the surface layer are indeed evident in the O *K* fine structure profile as shown in Fig. 3 and the inset graph, respectively. We can thus conclude that the oxidation state of the Fe is reduced owing to oxygen deficiency at the surface.

The properties of Fe-based compounds vary widely with the oxidation state of Fe [58-61]. Hence, to understand the effect of surface reduction of the film on its electronic and magnetic properties we used DFT calculations. While the superlattice contains a nominal amount of $SrFeO_3$, it is evident from STEM-EELS (Fig. 2(c)) that Fe remains in 3+ oxidation state in the bulk of the film except for ~1 unit cell regions around the $SrFeO_3$ layers. Moreover from STEM imaging, we find both the interface with $SrTiO_3$ and the surface of the film are terminated with a LaO layer. Therefore, we investigated the electronic properties of symmetric $LaFeO_3$ slabs with both surfaces terminated with LaO layer as shown in Fig. 4(a), which results in an overall La-rich stoichiometry.

From a purely ionic scenario, La donates three valence electrons and oxygen accepts two. Each LaO layer therefore donates $1e^-$ that is shared equally by its two neighboring FeO_2 layers. The extra LaO layer in the slab, therefore, contributes an additional $0.5e^-$ per unit cell. As shown in the layer-resolved 3*d* density of states (DOS) of Fe in the three different layers in Fig. 4(a), we find the extra $0.5e^-$ per unit cell to be confined to the surface unit cell, which includes the LaO surface layer and the sub-surface FeO_2 layer. In bulk $LaFeO_3$, Fe^{3+} is present in a high-spin state with octahedral coordination and the five *d*-electrons occupy three t_{2g} and two e_g states in one spin-channel with the conduction-band minima being made up of empty t_{2g} states in the other spin-channel. The half electron per unit cell donated by the extra LaO surface layer can in principle be shared equally by the Fe atoms in the surface unit cell, which would result in a metallic state with one of the *d*-states being half-filled. However, we find that the system undergoes a charge ordering with one electron being shared by every other Fe atom as shown in the spin isosurface of the occupied surface state in Fig. 4(b), which leads in an overall insulating state. Thus, half of the Fe atoms in the surface unit cell are in Fe^{2+} state, with the remaining half in Fe^{3+} oxidation state and, as guided by Goodenough-Kanamori rules [62,63], the magnetic ordering of the slab due to Fe^{3+}–O–Fe^{3+} and Fe^{2+}–O–Fe^{3+} superexchange interactions remains G-type antiferromagnetic (AFM) as that of bulk $LaFeO_3$ [48].

Oxide surfaces are prone to the formation of oxygen vacancies [64-66] and as discussed above, we also observe the presence of oxygen vacancies at the surface of the superlattice film from O *K* edge EELS. In order to reduce the surface layer to Fe^{2+} as observed in EELS, we introduced oxygen vacancies to the surface unit cell of the slab. Every oxygen vacancy introduces two electrons to the system, whereby we need an additional $0.5e^-$ per unit cell to achieve a surface oxidation state of 2+. We use (2×2) slabs in our calculations with four Fe and eight O atoms in every FeO_2 layer. Consequently, we need one oxygen vacancy (V_O) for each surface of the slab to achieve a surface oxidation state Fe^{2+}, or a vacancy concentration per unit cell area, $n_V = 0.25$. We find the formation energy of creating a vacancy in the surface LaO layer to be ~1 eV higher than creating one in the sub-surface FeO_2 layer. Figure 4(c) shows the structure of the slab with $n_V = 0.25$. Even in the presence of the vacancy, the FeO_x polyhedra tilts

persist for the surface layer in agreement with the STEM ABF images in Fig. 1(b). We find the additional electrons from the oxygen vacancy completely occupy one of the three t_{2g} states for all the surface Fe atoms as shown in the layer-resolved DOS in Fig. 4(c) (thus reducing them to Fe^{2+}) and overall the slab remains insulating with G-type AFM ordering as shown in the spin isosurface in Fig. 4(d).

Oxygen vacancies at $SrTiO_3$ surfaces have been proposed to lead to the formation of 2DEG at the surface [2]. In order to examine if such a metallic behavior could also be achieved in the $LaFeO_3$ slabs, we systematically introduced additional oxygen vacancies in the surface unit cell. As shown in the Supplemental Material (Fig. S3), we find that the formation energy for creating additional surface vacancies to be small (within 0.5 eV from the formation energy of $n_V = 0.25$), which suggests it is energetically possible to add more vacancies by varying the partial pressure of oxygen in experiments. We also find the vacancies to be energetically more favorable to form in the sub-surface FeO_2 layer than the surface LaO layer for all concentrations.

The inclusion of additional vacancies, however, leads to significant changes in the electronic and magnetic behavior of the surfaces. On adding two vacancies or $n_V = 0.5$, the system still maintains an overall insulating state, with the additional electrons occupying the empty t_{2g} states of the Fe atoms in the second unit cell from the surface. The electronic structure for different vacancy concentrations is discussed in Supplemental Materials (Fig. S4). Here we focus on the case with four vacancies or $n_V = 1$. As shown in Fig. 5(a), the four vacancies have been ordered in a fashion such that they form a corner-connected tetrahedral network around the Fe atoms, which is commonly observed in the brownmillerite structure [67]. The change from octahedral to tetrahedral coordination also changes the ordering of the crystal-field split Fe *d*-states with e_g states moving to lower energy compared to t_{2g} states under tetrahedral coordination as can be seen for the surface layer-resolved DOS in Fig. 5(b).

The change from octahedral to tetrahedral coordination in bulk Fe-compounds is often associated with changes in magnetic ordering, such as in magnetite Fe_3O_4 [68]. Hence, we carried out further calculations to find the ground-state magnetic configuration of the slab with reduced tetrahedrally coordinated surfaces. Indeed, we find the most stable magnetic ordering to be the case where the surface Fe moments align ferromagnetically, while the bulk moments remain G-type antiferromagnetically ordered, as shown in Fig. 5(a). The difference in energy of the surface ferromagnetic (FM) and G-type AFM configuration is plotted in Fig. 5(c) for different vacancy concentrations. We find a transition from antiferromagnetic to ferromagnetic ordering of the surface moments for n_V between 0.5 and 0.75, using both GGA and GGA+*U* approaches. Furthermore, for $n_V = 1$, the surface FM structure is found to be robust compared to G-type AFM ordering with an energy difference of ~40 meV (60 meV) per iron atom, calculated by using GGA+*U* (GGA).

Moreover, we find that the transition to the surface FM structure also leads to half-metallic surface states (of e_g character) as shown in the layer-resolved DOS in Fig. 5(b), while the bulk of the slab remains insulating, thus resulting in a spin-polarized 2DEG that is confined to the surface unit cell. From the spin isosurface for the occupied surface states shown in Fig. 5(d), we find that the electrons are localized in between iron sites (at the oxygen vacancies), which suggests that ferromagnetism arises due to coupling through the e_g conduction electrons as opposed to the double-exchange mechanism mediated through oxygen 2*p* states that is commonly observed in half-metallic perovskites [69,70].

4. Conclusion

In conclusion, we predict the formation of a spin-polarized 2DEG at the surface of (001) $LaFeO_3$ surface terminated with a LaO layer when excess surface oxygen vacancies are present. Based on STEM-EELS, we show that Fe is reduced to 2+ and the surface reduction is confined to four unit cells at the surface. We find that the additional electrons due to the reduction are confined to the surface region. We find that further reduction of the surface region results in filling up of unoccupied e_g states along with a transition to half-metallic surface state wherein the moments of the surface Fe-atoms are aligned ferromagnetically, while the bulk layers remain antiferromagnetic and insulating. We, therefore, propose that it might be possible to achieve a spin-polarized 2DEG on LaO-terminated $LaFeO_3$ surfaces by changing the partial pressure of oxygen. Based upon our observation that the half-metallic surface states are observed over a large filling of e_g occupancy, it might also be possible to achieve such a novel behavior on reduced surfaces of other perovskite transition-metal oxides.

Acknowledgments

Work at ORNL was supported by the Department of Energy (DOE) Office of Science, Office of Basic Energy Sciences (BES), Materials Science and Engineering Directorate and through user projects supported by ORNL's Center for Nanophase Materials Sciences, which is sponsored by the Scientific User Facilities Division, Office of BES, U.S. DOE. YMK was supported by the Institute for Basic Science (IBS-R011-D1) in Korea. Work at Vanderbilt University is supported by DOE grant DE-FG02-09ER46554. Work at ANL was supported by the U.S. DOE, Office of BES, Materials Sciences and Engineering Division. Use of the Center for Nanoscale Materials, an Office of Science user facility, was supported by the U.S. DOE, Office of Science, Office of BES, under Contract No. DE-AC02-06CH11357. This work used computational resources of the National Energy Research Scientific Computing Center, which is supported by the Office of Science of the U.S. DOE under contract no. DE-AC02-05CH11231, and the Extreme Science and Engineering Discovery Environment (XSEDE), which is supported by National Science Foundation grant number ACI-1053575. We thank JQ Yan for the Fe^{2+} sample.

Figures

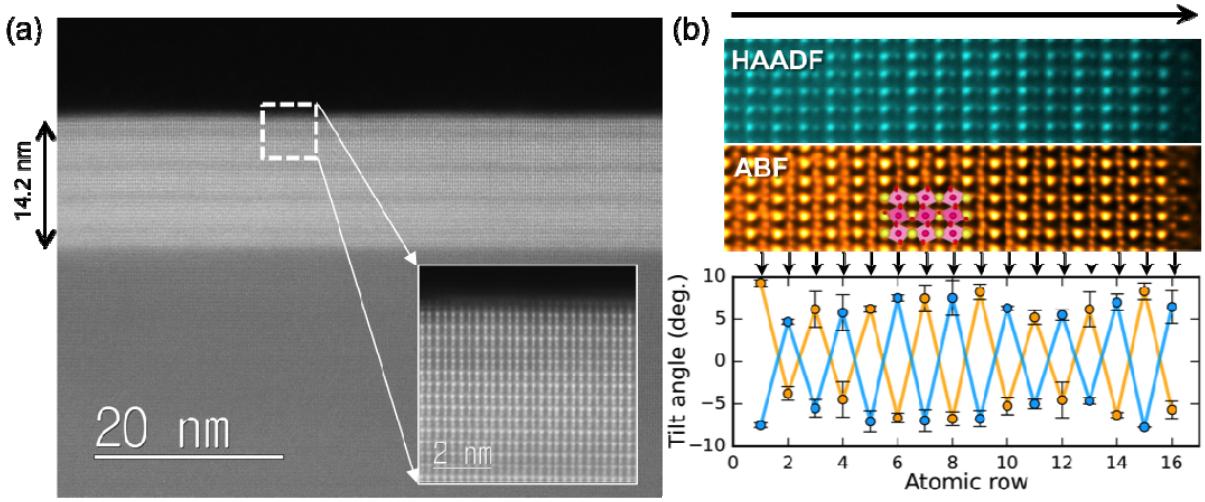

FIG. 1. (Color online) **Thin film structure, surface termination and octahedral tilt profile.** (a) HAADF STEM image of $[110]_{pc}$-oriented $(LaFeO_3)_8/(SrFeO_3)$ superlattice thin film grown on $SrTiO_3$ substrate. The inset shows the atomic structure of the surface the film. (b) A set of HAADF and ABF STEM images showing atomic column positions of the thin film up to the outermost surface layer (the arrow points towards the surface) and the profile of alternating oxygen octahedra rotations measured from the ABF STEM image.

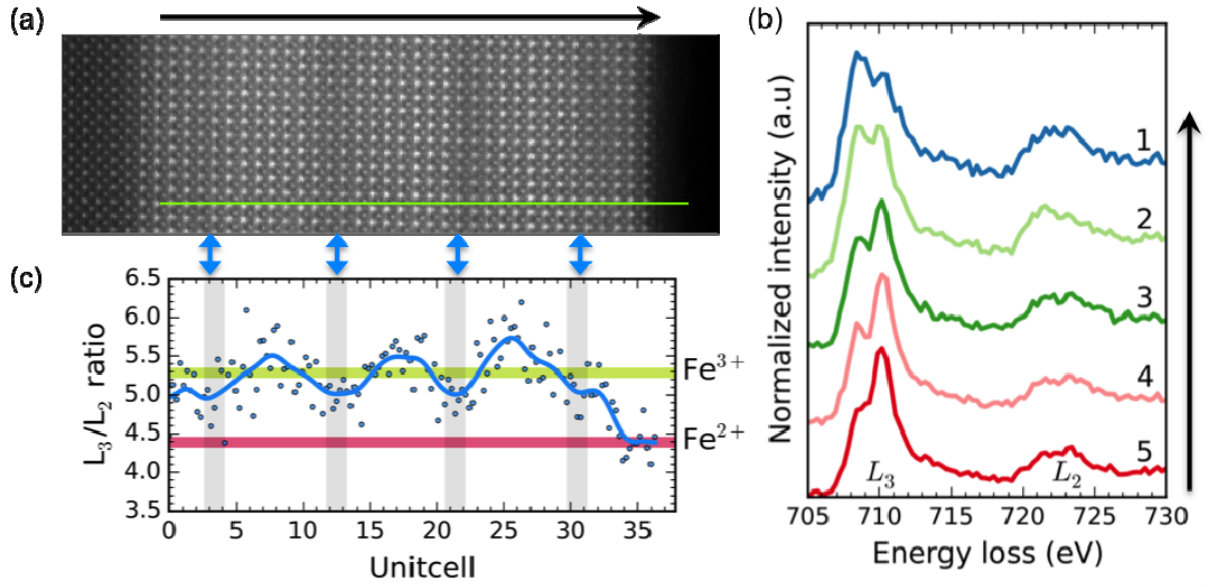

FIG. 2. (Color online) **Surface reduction from STEM EELS.** (a) HAADF image of the $[100]_{pc}$-oriented superlattice structure selected for core-loss EELS with the line showing the region from where the spectra was obtained. (b) EEL spectra of Fe *L* edge for the top five unit cells from the surface. (c) Change in the ratio of the L_3 to L_2 peak intensity of Fe (L_3/L_2 ratio) along the EELS line-scan. The horizontal regions shaded in green and pink show the L_3/L_2 ratio of standard specimens having Fe^{3+} and Fe^{2+}, respectively. The vertical regions shaded in grey highlight the $SrFeO_3$ layers in the superlattice. The black arrows point towards the surface.

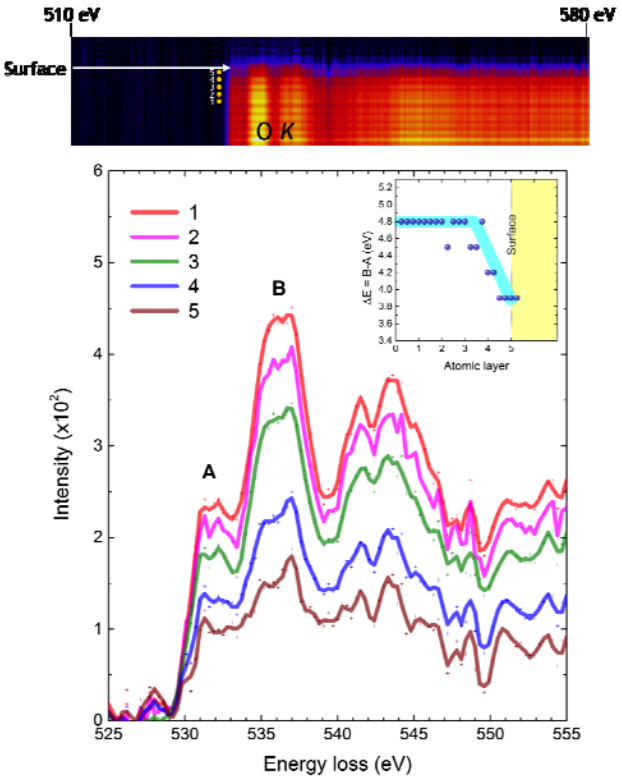

FIG. 3. (Color online) **EELS analysis of O *K* edge**. Comparison of O *K* edges obtained at the FeO_2 atomic layers from the inside of the film (numbered 1) to the outmost surface (numbered 5) from an EELS line-scan. The inset shows the decrease in separation between Peak B and A (ΔE) on moving towards the surface.

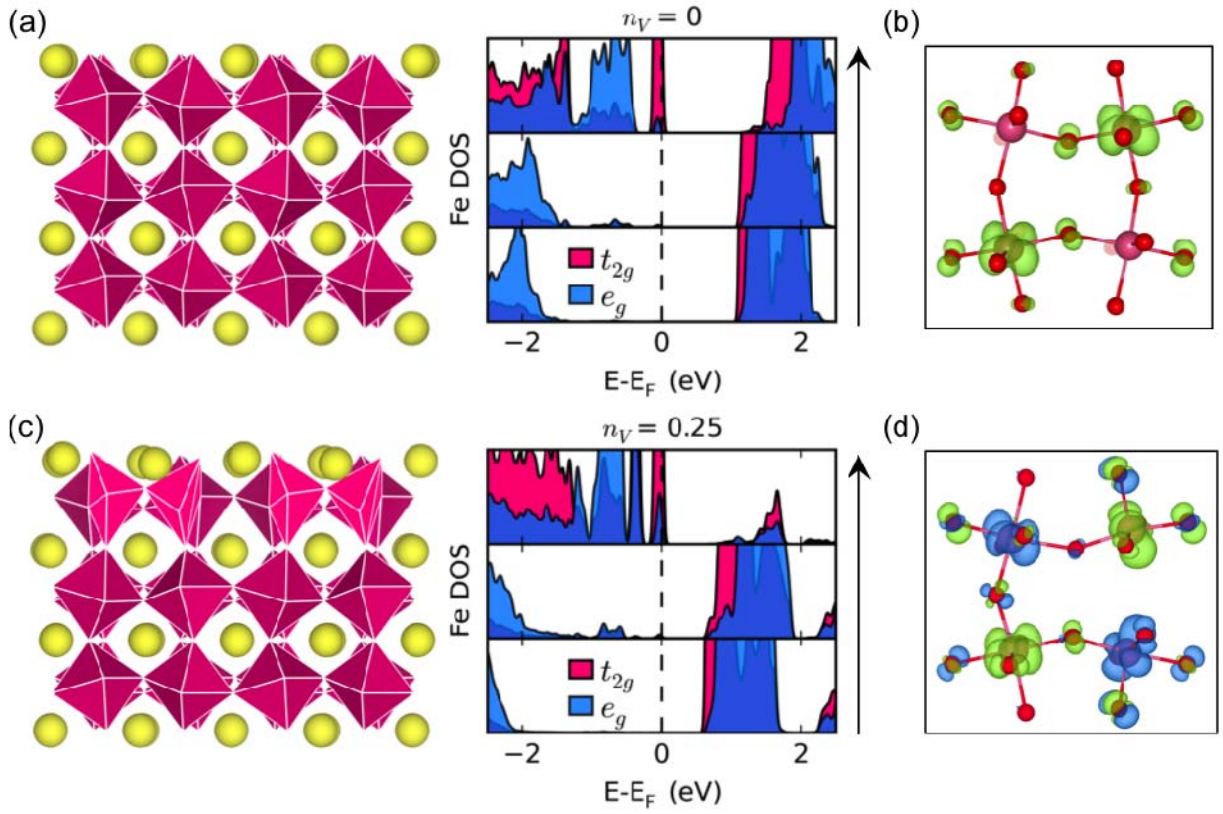

FIG. 4. (Color online) **Electronic structure of $LaFeO_3$ slabs with insulating surface.** (a) Structure of LaO-terminated $LaFeO_3$ slab showing the top three layers from the surface along with Fe-3*d* DOS for the corresponding layers. (b) Spin-isosurface showing charge ordering of Fe atoms in the sub-surface Fe-O layer of the slab shown in (a). (c) Structure of the $LaFeO_3$ slab with an oxygen vacancy concentration n_V = 0.25 in the sub-surface Fe-O layer along with Fe-3*d* DOS for the corresponding layers. (d) Spin-isosurface of the sub-surface Fe-O layer with n_V = 0.25.

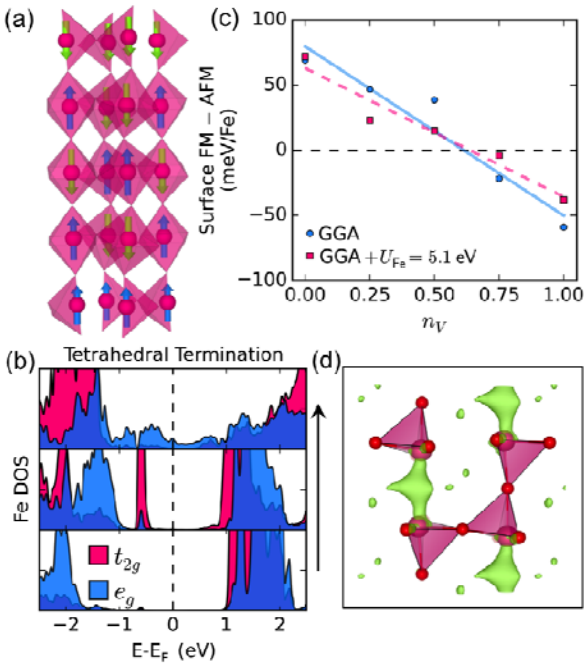

FIG. 5. (Color online) **Half-metallic ferromagnetism at the surface.** (a) Magnetic configuration of the $LaFeO_3$ slab with a vacancy concentration n_V = 1 in the sub-surface Fe-O layer. (b) Fe 3*d* DOS of the top three unit cells from the surface with the stable surface ferromagnetic configuration. (c) Difference in energy between the ferromagnetic and antiferromagnetic coupling of the surface Fe spins as a function of vacancy concentration in the sub-surface Fe-O layer. A negative energy corresponds to stable ferromagnetic configuration. (d) Spin-isosurface of the sub-surface Fe-O layer with n_V = 1 and with ferromagnetic ordering of surface Fe spins.

References

[1] H. Y. Hwang, Y. Iwasa, M. Kawasaki, B. Keimer, N. Nagaosa, and Y. Tokura, Nat Mater **11**, 103 (2012).
[2] A. F. Santander-Syro, O. Copie, T. Kondo, F. Fortuna, S. Pailhes, R. Weht, X. G. Qiu, F. Bertran, A. Nicolaou, A. Taleb-Ibrahimi, P. Le Fevre, G. Herranz, M. Bibes, N. Reyren, Y. Apertet, P. Lecoeur, A. Barthelemy, and M. J. Rozenberg, Nature **469**, 189 (2011).
[3] A. F. Santander-Syro, F. Fortuna, C. Bareille, T. C. Rodel, G. Landolt, N. C. Plumb, J. H. Dil, and M. Radovic, Nat Mater **13**, 1085 (2014).
[4] W. Meevasana, P. D. C. King, R. H. He, S. K. Mo, M. Hashimoto, A. Tamai, P. Songsiriritthigul, F. Baumberger, and Z. X. Shen, Nat Mater **10**, 114 (2011).
[5] M. Kim, C. Bell, Y. Kozuka, M. Kurita, Y. Hikita, and H. Y. Hwang, Physical Review Letters **107**, 106801 (2011).
[6] M. Bode, M. Heide, K. von Bergmann, P. Ferriani, S. Heinze, G. Bihlmayer, A. Kubetzka, O. Pietzsch, S. Blugel, and R. Wiesendanger, Nature **447**, 190 (2007).
[7] J. Suntivich, K. J. May, H. A. Gasteiger, J. B. Goodenough, and Y. Shao-Horn, Science **334**, 1383 (2011).
[8] J. Suntivich, H. A. Gasteiger, N. Yabuuchi, H. Nakanishi, J. B. Goodenough, and Y. Shao-Horn, Nat Chem **3**, 546 (2011).
[9] N. A. Spaldin and M. Fiebig, Science **309**, 391 (2005).
[10] S. V. Kalinin, A. Borisevich, and D. Fong, ACS Nano **6**, 10423 (2012).
[11] S. V. Kalinin and N. A. Spaldin, Science **341**, 858 (2013).
[12] S. V. Kalinin, D. A. Bonnell, T. Alvarez, X. Lei, Z. Hu, J. H. Ferris, Q. Zhang, and S. Dunn, Nano Letters **2**, 589 (2002).
[13] R. V. Wang, D. D. Fong, F. Jiang, M. J. Highland, P. H. Fuoss, C. Thompson, A. M. Kolpak, J. A. Eastman, S. K. Streiffer, A. M. Rappe, and G. B. Stephenson, Phys Rev Lett **102**, 047601 (2009).
[14] W. A. Saidi, J. M. Martirez, and A. M. Rappe, Nano Lett **14**, 6711 (2014).
[15] G. Binnig, H. Rohrer, C. Gerber, and E. Weibel, Physical review letters **49**, 57 (1982).
[16] M. Kawasaki, K. Takahashi, T. Maeda, R. Tsuchiya, M. Shinohara, O. Ishiyama, T. Yonezawa, M. Yoshimoto, and H. Koinuma, Science **266**, 1540 (1994).
[17] J. Shin, A. Y. Borisevich, V. Meunier, J. Zhou, E. W. Plummer, S. V. Kalinin, and A. P. Baddorf, ACS nano **4**, 4190 (2010).
[18] C. Renner, G. Aeppli, B.-G. Kim, Y.-A. Soh, and S.-W. Cheong, Nature **416**, 518 (2002).
[19] A. Tselev, R. K. Vasudevan, A. G. Gianfrancesco, L. Qiao, P. Ganesh, T. L. Meyer, H. N. Lee, M. D. Biegalski, A. P. Baddorf, and S. V. Kalinin, ACS nano.
[20] R. K. Vasudevan, A. Tselev, A. G. Gianfrancesco, A. P. Baddorf, and S. V. Kalinin, Applied Physics Letters **106**, 143107 (2015).
[21] J. A. Enterkin, A. K. Subramanian, B. C. Russell, M. R. Castell, K. R. Poeppelmeier, and L. D. Marks, Nat Mater **9**, 245 (2010).
[22] N. Erdman, K. R. Poeppelmeier, M. Asta, O. Warschkow, D. E. Ellis, and L. D. Marks, Nature **419**, 55 (2002).
[23] C. H. Lanier, J. M. Rondinelli, B. Deng, R. Kilaas, K. R. Poeppelmeier, and L. D. Marks, Phys Rev Lett **98**, 086102 (2007).
[24] N. Shibata, A. Goto, S. Y. Choi, T. Mizoguchi, S. D. Findlay, T. Yamamoto, and Y. Ikuhara, Science **322**, 570 (2008).
[25] M. Matsukawa, R. Ishikawa, T. Hisatomi, Y. Moriya, N. Shibata, J. Kubota, Y. Ikuhara, and K. Domen, Nano letters **14**, 1038 (2014).
[26] G. Z. Zhu, G. Radtke, and G. A. Botton, Nature **490**, 384 (2012).
[27] D. Kienzle, P. Koirala, and L. D. Marks, Surface Science **633**, 60 (2015).
[28] S. J. Pennycook and P. D. Nellist, *Scanning transmission electron microscopy: imaging and analysis* (Springer Science & Business Media, 2011).

[29] M. Varela, M. P. Oxley, W. Luo, J. Tao, M. Watanabe, A. R. Lupini, S. T. Pantelides, and S. J. Pennycook, Physical Review B **79** (2009).
[30] P. A. van Aken and B. Liebscher, Physics and Chemistry of Minerals **29**, 188 (2002).
[31] C. C. Ahn and P. Rez, Ultramicroscopy **17**, 105 (1985).
[32] P. E. Blöchl, Physical Review B **50**, 17953 (1994).
[33] G. Kresse and J. Hafner, Phys Rev B Condens Matter **47**, 558 (1993).
[34] G. Kresse and J. Hafner, Physical Review B **49**, 14251 (1994).
[35] J. P. Perdew, K. Burke, and M. Ernzerhof, Physical Review Letters **77**, 3865 (1996).
[36] H. J. Monkhorst and J. D. Pack, Physical Review B **13**, 5188 (1976).
[37] V. V. Anisimov, J. Zaanen, and O. K. Andersen, Phys Rev B Condens Matter **44**, 943 (1991).
[38] S. L. Dudarev, G. A. Botton, S. Y. Savrasov, C. J. Humphreys, and A. P. Sutton, Physical Review B **57**, 1505 (1998).
[39] J. Hong, A. Stroppa, J. Íñiguez, S. Picozzi, and D. Vanderbilt, Physical Review B **85**, 054417 (2012).
[40] A. M. Ritzmann, A. B. Muñoz-García, M. Pavone, J. A. Keith, and E. A. Carter, Chemistry of Materials **25**, 3011 (2013).
[41] Y.-L. Lee, J. Kleis, J. Rossmeisl, and D. Morgan, Physical Review B **80** (2009).
[42] K. Reuter and M. Scheffler, Physical Review B **65** (2001).
[43] K. Garrity and S. Ismail-Beigi, Physical Review B **80**, 085306 (2009).
[44] K. Garrity, A. Kakekhani, A. Kolpak, and S. Ismail-Beigi, Physical Review B **88** (2013).
[45] X. Huang, B. Wang, E. A. Grulke, and M. J. Beck, The Journal of Chemical Physics **140**, 074703 (2014).
[46] R. Ishikawa, E. Okunishi, H. Sawada, Y. Kondo, F. Hosokawa, and E. Abe, Nat Mater **10**, 278 (2011).
[47] Q. He, R. Ishikawa, A. R. Lupini, L. Qiao, E. J. Moon, O. Ovchinnikov, S. J. May, M. D. Biegalski, and A. Y. Borisevich, Acs Nano **9**, 8412 (2015).
[48] W. C. Koehler and E. O. Wollan, Journal of Physics and Chemistry of Solids **2**, 100 (1957).
[49] R. Mishra, Y. M. Kim, J. Salafranca, S. K. Kim, S. H. Chang, A. Bhattacharya, D. D. Fong, S. J. Pennycook, S. T. Pantelides, and A. Y. Borisevich, Nano Lett **14**, 2694 (2014).
[50] C. Colliex, T. Manoubi, and C. Ortiz, Physical Review B **44**, 11402 (1991).
[51] See Supplemental Material at http://link.aps.org/supplemental/10.1103/ for details of the standard compounds and additional data from STEM-EELS experiments and DFT calculations.
[52] A. Feldhoff, J. Martynczuk, M. Arnold, M. Myndyk, I. Bergmann, V. Šepelák, W. Gruner, U. Vogt, A. Hähnel, and J. Woltersdorf, Journal of Solid State Chemistry **182**, 2961 (2009).
[53] F. M. F. de Groot, M. Grioni, J. C. Fuggle, J. Ghijsen, G. A. Sawatzky, and H. Petersen, Phys Rev B **40**, 5715 (1989).
[54] H. Kurata and C. Colliex, Phys Rev B **48**, 2102 (1993).
[55] L. F. Kourkoutis, H. L. Xin, T. Higuchi, Y. Hotta, J. H. Lee, Y. Hikita, D. G. Schlom, H. Y. Hwang, and D. A. Muller, Philos. Mag. **90**, 4731 (2010).
[56] W. Luo, M. Varela, J. Tao, S. J. Pennycook, and S. T. Pantelides, Phys Rev B **79**, 052405 (2009).
[57] C. Cantoni, J. Gazquez, F. Miletto Granozio, M. P. Oxley, M. Varela, A. R. Lupini, S. J. Pennycook, C. Aruta, U. S. di Uccio, P. Perna, and D. Maccariello, Adv Mater **24**, 3952 (2012).
[58] E. J. Verwey, P. W. Haayman, and F. C. Romeijn, Journal of Chemical Physics **15**, 181 (1947).
[59] C. H. Yang, J. Seidel, S. Y. Kim, P. B. Rossen, P. Yu, M. Gajek, Y. H. Chu, L. W. Martin, M. B. Holcomb, Q. He, P. Maksymovych, N. Balke, S. V. Kalinin, A. P. Baddorf, S. R. Basu, M. L. Scullin, and R. Ramesh, Nature Materials **8**, 485 (2009).
[60] Y. Xie, M. D. Scafetta, R. J. Sichel-Tissot, E. J. Moon, R. C. Devlin, H. Wu, A. L. Krick, and S. J. May, Advanced Materials **26**, 1434 (2014).
[61] Y. J. Xie, M. D. Scafetta, E. J. Moon, A. L. Krick, R. J. Sichel-Tissot, and S. J. May, Applied Physics Letters **105**, 062110 (2014).
[62] J. B. Goodenough, Physical Review **100**, 564 (1955).

[63] J. Kanamori, Journal of Physics and Chemistry of Solids **10**, 87 (1959).
[64] D. W. Reagor and V. Y. Butko, Nat Mater **4**, 593 (2005).
[65] B. M. Pabón, J. I. Beltrán, G. Sánchez-Santolino, I. Palacio, J. López-Sánchez, J. Rubio-Zuazo, J. M. Rojo, P. Ferrer, A. Mascaraque, M. C. Muñoz, M. Varela, G. R. Castro, and O. R. de la Fuente, Nat Commun **6** (2015).
[66] M. D. Rossell, P. Agrawal, A. Borgschulte, C. Hébert, D. Passerone, and R. Erni, Chemistry of Materials **27**, 3593 (2015).
[67] P. D. Battle, T. C. Gibb, and P. Lightfoot, Journal of Solid State Chemistry **84**, 237 (1990).
[68] J. P. Wright, J. P. Attfield, and P. G. Radaelli, Physical Review Letters **87**, 266401 (2001).
[69] C. Zener, Physical Review **81**, 440 (1951).
[70] C. Zener, Physical Review **82**, 403 (1951).